A decade of atom-counting in STEM : from the first results toward reliable 3D atomic models from a single projection

A decade of atom-counting in STEM: from the first results toward reliable 3D atomic models from a single projection

A. De Backer[a,b,*], S. Bals[a,b], S. Van Aert[a,b]

[a] *Electron Microscopy for Materials Science (EMAT), University of Antwerp, Groenenborgerlaan 171, 2020 Antwerp, Belgium*
[b] *NANOlab Center of Excellence, University of Antwerp, Groenenborgerlaan 171, 2020 Antwerp, Belgium*

Abstract

Quantitative structure determination is needed in order to study and understand nanomaterials at the atomic scale. Materials characterisation resulting in precise structural information is a crucial point to understand the structure-property relation of materials. Counting the number of atoms and retrieving the 3D atomic structure of nanoparticles plays an important role here. In this paper, an overview will be given of the atom-counting methodology and its applications over the past decade. The procedure to count the number of atoms will be discussed in detail and it will be shown how the performance of the method can be further improved. Furthermore, advances toward mixed element nanostructures, 3D atomic modelling based on the atom-counting results, and quantifying the nanoparticle dynamics will be highlighted.

1. Introduction

During his rich career, John Spence has spent a major part striving to image atoms for solving materials science questions. Witness to this is the publication of his book 'High resolution electron microscopy' that is read by many young scientists and microscopists. The first direct observation of individual atoms was with a scanning transmission electron microscopy (STEM) set-up in the early seventies [1]. After this observation, many efforts have been made to reach ultra high resolution in TEM. However, Spence also foresaw that the STEM set-up, although unforeseeably in the nineties of the previous century, would be promising because of the Z-contrast [2]. In our research field, this prognosis is more than fulfilled as we are nowadays extensively exploiting the Z- and thickness-contrast of the atomic resolution annular dark field (ADF) STEM images for quantitative analyses. Unlike qualitative methods which are based on a visual interpretation of the acquired images, quantitative methods enable to determine the chemical composition at a local scale [3–5] and to measure the atom positions down to picometer precision [6–9]. For this purpose, electron microscopy images are treated as datasets from which unknown structure parameters can be measured. To reach this goal, statistical parameter estimation theory is introduced in the field of atomic resolution electron microscopy [10–12]. This approach enables us to quantify atomic column positions and the total intensity of scattered electrons for each atomic column, from atomic resolution ADF STEM images. The latter is the so-called scattering cross-section which is robust to defocus, source size, magnification, and small sample mis-tilt [3, 13–15]. Furthermore these scattering cross-sections increase monotonically with thickness and the atomic number Z. When further analysing the distribution of the scattering cross-sections with advanced quantification procedures, the number and/or type of atoms can be measured [16–18]. In tribute to John Spence, we give an overview of a decade of atom-counting from ADF STEM images. In section 2, we introduce our statistics based atom-counting method which was introduced back in 2011 for the first time. In addition, we propose a modified model for the description of the distribution of the scattering cross-section values, which will improve the accuracy of the obtained atom-counting results. Section 3 discusses the possibilities to unscramble the number of atoms in mixed element nanostructures. Next in section 4, it is shown how the atom-counting results can be used to retrieve the atomic structure in three dimensions (3D). An overview is given from the first initial results up to more advanced reconstruction methods, allowing to retrieve reliable atomic models based on atom-counting results from a single viewing direction. Finally, in section 5, the opportunities to study nanoparticle dynamics are considered.

2. Nanoparticle atom-counting

As mentioned in the introduction, atomic resolution HAADF STEM images are both sensitive to the composition and thickness of each atomic column. The latter enables us to count the number of atoms in each atomic column for homogeneous nanoparticles. Different methods have been introduced over the past years [16–23]. Here, our statistics-based atom-counting method will be illustrated for a Au nanorod [17]. Fig. 1(a) shows an aberration-corrected high angle (HA)ADF STEM image of the Au nanorod viewed along the [100] zone-axis. Using statistical parameter estimation theory, the experimental observations are considered as a data plane from which the unknown structure parameters are estimated. For an atomic resolution ADF STEM image, the unknown structure pa-

*sandra.vanaert@uantwerpen.be

rameters are the atomic column positions and the scattering cross-section values for each atomic column. The key to the successful application of this approach is the availability of a parametric model which describes the pixel values in the ADF STEM image. Since the intensity is often sharply peaked at the atomic column positions, atomic resolution (S)TEM images are modelled as a superposition of Gaussian peaks [10–12]. The locations of the Gaussian peaks correspond to the atomic column positions and the volume under the Gaussian peaks equals the scattering cross-section, which is sensitive to the number of atoms. The parametric model consisting of a superposition of Gaussian peaks is fitted to the experimental ADF STEM image using the uniformly weighted least squares criterion. This criterion quantifies the similarity between the experimental data and the model. An efficient implementation of this algorithm is available in the StatSTEM software package [12]. The refined parametrised model is shown in Fig. 1(b), showing a close match with the experimental data.

Based on the estimated parameters, the scattering cross-sections are determined for each atomic column and these are shown in the histogram in Fig. 1(e). Ideally, the histogram of scattering cross-sections for all atomic columns in this image would consist of isolated components where each component corresponds to a set of atomic columns having the same number of atoms in it. In practice, however, the components are smeared out due to a combination of experimental detection noise and the environment. Therefore these results cannot be interpreted directly in terms of the number of atoms in a column. In order to retrieve then the number of components and their locations, a combination of a so-called Gaussian mixture model and an order selection criterion is used [18, 24]. An additional advantage is that the result only depends on the values of the estimated scattering cross-sections and is independent of the subjective choice of bins in the histogram. The order selection criterion indicates the number of statistically significant components in the underlying scattering cross-sections measures. The number of components corresponds to a minimum in the evaluation of this criterion as a function of the number of components as illustrated in Fig. 1(d). Often this corresponds to a local minimum. For this Au nanorod, 47 components are present, suggesting that the number of atoms varies from 1 up to 47 atoms. The Gaussian mixture model analysis defines the positions, the width, and the proportion of each Gaussian component. The scattering cross-section of each atomic column can then be assigned to the component having the largest probability for this scattering cross-section, leading to a map reflecting the number of atoms for each atomic column as shown in Fig. 1(c).

Since many local minima are present in the order selection criterion shown in Fig. 1(d), a validation step is often required. This is possible through a comparison with image simulations. For this purpose, the intensities in the ADF STEM image have been normalised with respect to the incident beam [25–27] allowing one to directly compare the experimental and simulated scattering cross-section values. Fig. 1(f) shows the experimental mean scattering cross-sections - corresponding to the component locations in Fig. 1(e) - together with the scattering cross-sections estimated from frozen phonon calculations performed under the same experimental conditions [28]. The excellent match of the experimental and simulated intensities within the expected 5%–10% error range validates the accuracy of the obtained atom counts [4, 19].

Up to now, the components of the Gaussian mixture model shown in Fig. 1(e) are modelled as homoscedastic components, i.e. components with a common width. Ultimately, the images from which the scattering cross-sections are estimated, contain only Poisson noise. In this dose-limited case, the variance of the components cannot be considered as homoscedastic any more. The variance of the scattering cross-sections then depends on the dose and the scattering cross-section value [29]. A homoscedastic model will then fail to correctly describe the distribution of the scattering cross-section values. In order to improve the accuracy of the atom-counting results at low doses for which the dose dependent behaviour is most dominant, we propose to include the dose-dependent width from Van Aert et al. [29] in the Gaussian mixture model next to a dose-independent width. The effective width of the normal components is then given by:

$$\sigma_{\text{eff}} = \sqrt{\sigma_{di} + \sigma_d} = \sqrt{\sigma_{di} + \frac{\mu_g}{d}}. \tag{1}$$

The parameters σ_{di} and σ_d denote the dose-independent and dose-dependent contributions to the width; μ_g is the location of the gth component and d is the incoming electron dose. It is important to note that the dose-dependent width, i.e. μ_g/d increases with increasing thickness. The mixture model with G components is then described by:

$$f_{\text{mix}}(SCS_n; \mathbf{\Psi}_G) = \sum_{g=1}^{G} \frac{\pi_g}{\sqrt{2\pi}\sigma_{\text{eff}}} \exp\left(-\frac{(SCS_n - \mu_g)^2}{2\sigma_{\text{eff}}}\right) \tag{2}$$

where SCS_n represents the stochastic variable for the $n$the scattering cross-section. The symbol $\mathbf{\Psi}_G$ represents the unknown parameters in the mixture model with G components:

$$\mathbf{\Psi}_G = (\pi_1, \ldots, \pi_{G-1}, \mu_1, \ldots, \mu_G, \sigma_{\text{di}})^T \tag{3}$$

where parameter π_g denotes the mixing proportion of the gth component. The parameters given by Eq.(3), are estimated using the expectation maximisation algorithm, described in [18, 30].

In order to evaluate the improvement for the atom-counting analysis, 1000 noise realisations of 240 scattering cross-section values coming from a mixture model with 12 components and with equal proportions have been generated at different doses, ranging from 10^3 $e^-/\text{Å}^2$ to 10^5 $e^-/\text{Å}^2$. The locations of the 12 components correspond to the ADF STEM scattering cross-sections that can be expected for 1 up 12 Au atoms imaged with an aberration corrected ADF STEM set-up at an acceleration voltage of 300 kV, a probe convergence of 20 mrad and a annular detector ranging over 45-180 mrad. The dose-independent width σ_{di} equals either 0 or 0.0042. The latter value mimics the

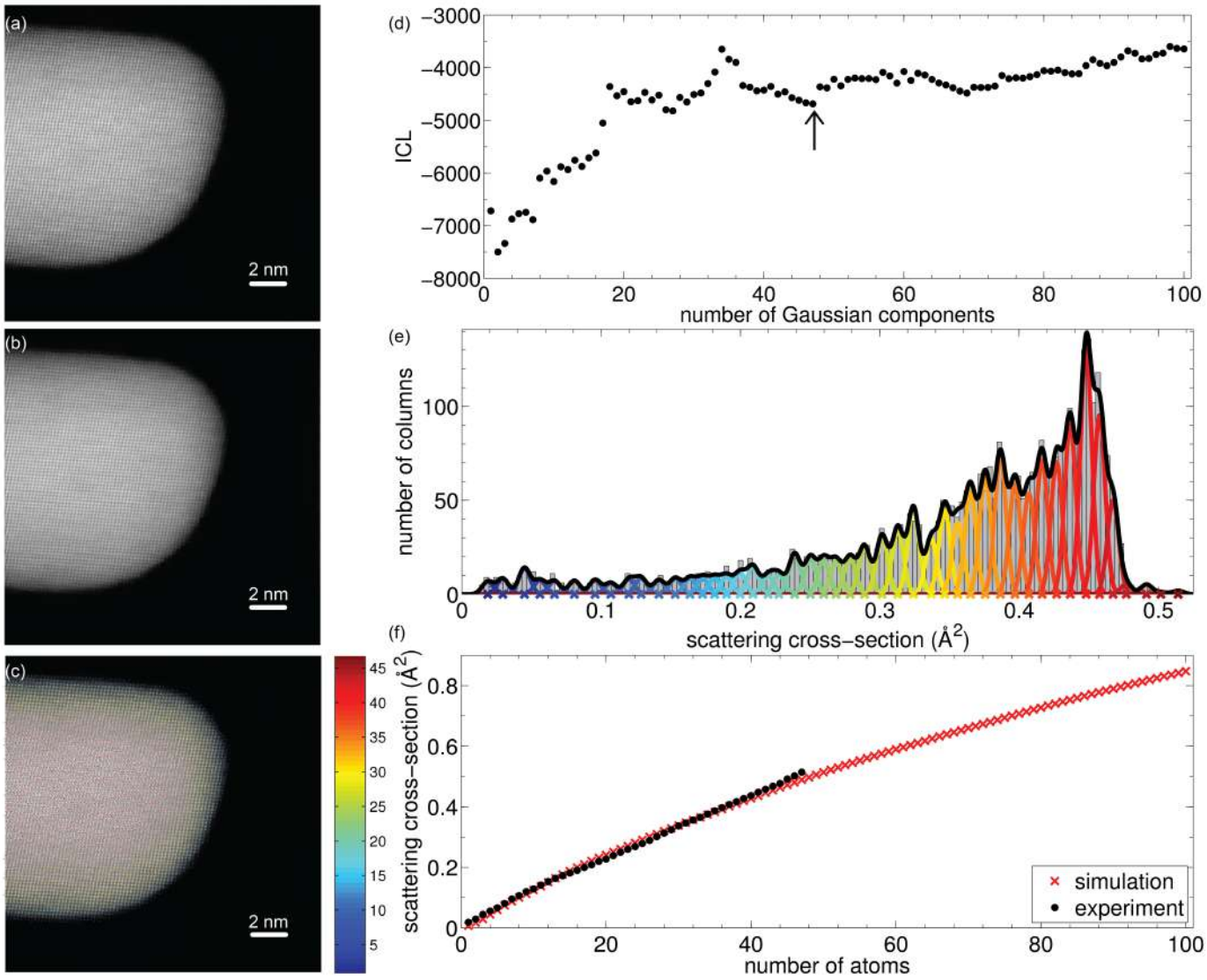

Figure 1: (a) Experimental HAADF STEM image of an Au nanorod. (b) Refined parametrised model. (c) The number of Au atoms per column. (d) ICL criterion evaluated as a function of the number of Gaussians in a mixture model. (e) Histogram of scattering cross-sections of the Au columns, together with the estimated mixture and its individual components. (f) Comparison of experimental and simulated scattering cross-sections. Adapted figure with permission from [17] Copyright (2013) by the American Physical Society.

contributions from scan noise distortions. Two types of Gaussian mixture models are estimated for each simulated dataset: a homoscedastic model and the mixture model of Eq. (2) containing the effective width introduced in Eq. (1). The performance of both approaches is evaluated in terms of the correctly identified number of components by assessing the ICL criterion. The results are shown in Fig. 2(a). It is clear that the fraction of correctly identified number of components is significantly increased for the new model including the dose-dependent width (blue curves). The improved performance is most pronounced for the underlying distribution with $\sigma_{di} = 0$. In the presence of a dose-independent contribution and at higher doses, the original homoscedastic model also shows a good performance. Nowadays, with the availability of more stable instruments and software to correct for e.g. scan noise distortions [31], we are closer to the dose-limited regime and the accuracy of the atom-counting results will benefit of the improved model. The reason for the misidentification of the number of components is further illustrated in Fig. 2(b-d) for one simulated distribution. The same trend will be observed for other noise realisations as well. Fig. 2(b) shows an example of the ICL criteria for a simulated distribution with an incoming electron dose of $3 \cdot 10^3$ $e^-/\text{Å}^2$ and $\sigma_{di} = 0$. The ICL evaluation of the dose dependent models correctly identified 12 components, however, the evaluation for the homoscedastic models indicates more components, i.e. in this case 14 components. From the mixture models, it is clear that the homoscedastic model includes extra components to model the increased variety in the scattering cross-section values for the components corresponding to higher number of atoms (Fig. 2(c)). Indeed, from a detailed comparison of the models in Figs. 2(c) and (d), it can be seen that the last three components in Fig. 2(d) are split into five components in the ho-

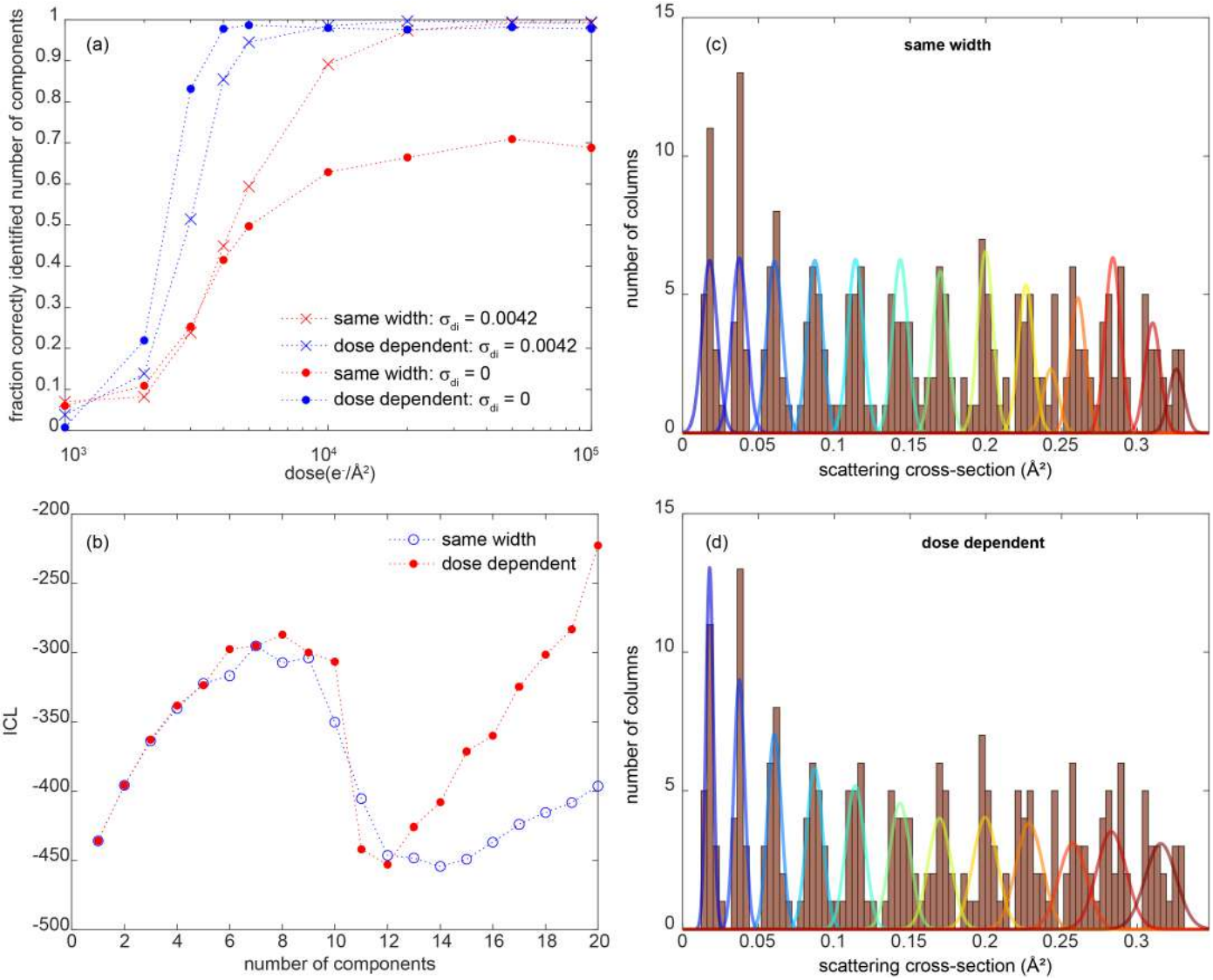

Figure 2: Comparison of the performance of the Gaussian mixture models with the same width and dose-dependent width. (a) Fraction of correctly identified number of components as a function of the incident electron dose based on the estimated models with the same width and dose-dependent width for underlying simulated distributions with $\sigma_{di} = 0.0042$ and $\sigma_{di} = 0$. (b) Example of an ICL criterion for the homoscedastic and dose-dependent models for an incoming electron dose of $3 \cdot 10^3$ $e^-/\text{Å}^2$ with $\sigma_{di} = 0$. (c) Estimated homoscedastic Gaussian mixture model for 14 components corresponding to the minimum in (b). (d) Estimated dose-dependent Gaussian mixture model for 12 components corresponding to the minimum in (b).

moscedastic model in Fig. 2(d). The homoscedastic model will systematically overestimate the number of components resulting in the a lower performance shown in Fig. 2(a). The novel model retrieves the correct number of components and models more accurately the underlying distribution of scattering cross-section values (Fig. 2(d)).

3. From homogeneous to heterogeneous

In the previous section, atom-counting was discussed for nanoparticles consisting of a single type of element. However, many relevant materials often consist of more than one chemical element because of their unique electronic, optical, or catalytic properties . For mixed element columns, all types of elements will contribute differently to the scattering cross-section thus significantly complicating atom-counting as compared to monotype nanostructures. Therefore, image simulations play an important role to access the number and type of atoms in each atomic column. Since small changes in the atom ordering in the column can modify the scattering cross-sections, the amount of required simulations makes it almost an impossible task in terms of computing time. Indeed, already more than 2×10^6 simulations would be needed for a 20 atoms thick binary alloy having all possible ratios between both elements. Therefore, a non-linear model, capable of predicting scattering cross-sections in terms of the 3D atomic arrangement was developed by taking dynamical electron diffraction into account [32, 33]. In this so-called atomic lensing model, the lensing effect of scattering cross-sections is modelled as a superposition of individual atoms focusing the incoming electrons as schematically

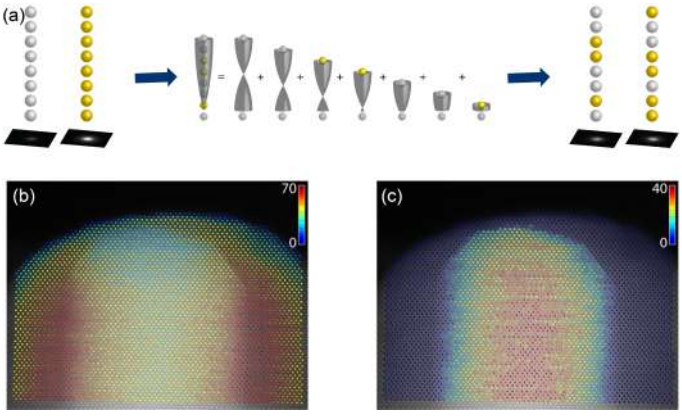

Figure 3: (a) Illustration of the atomic lensing model: the lensing effect of the scattering cross-sections is modelled as a superposition of individual atoms focusing the incoming electrons. (b) The number of Ag atoms in an experimental HAADF STEM image of a Ag-coated Au nanorod (c) The number of Au atoms counted from the same experimental HAADF STEM image. Adapted with permission from [32] Copyright (2016) by the American Physical Society.

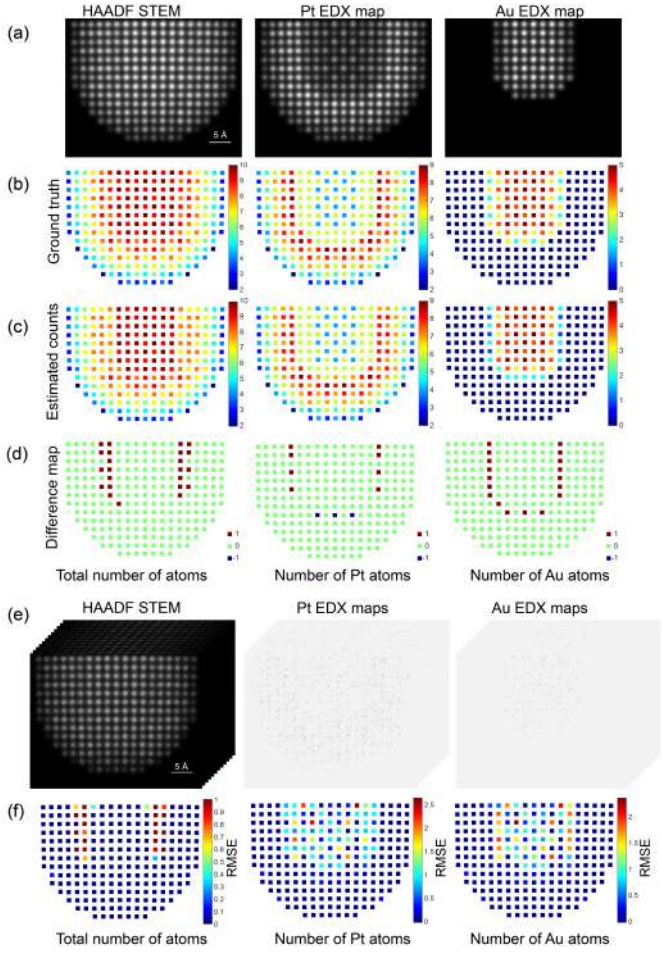

Figure 4: Simulated HAADF STEM image and EDX elemental maps of an Au@Pt core–shell nanorod, together with the ground truth atom counts, the estimated atom-counts, and the difference maps for the total number of atoms and both the number of Pt and Au atoms in an atomic column. Adapted figure with permission from [34] Copyright (2022) John Wiley and Sons.

illustrated in Fig. 3(a). This model enables predicting scattering cross-sections of any mixed column of atoms based on the scattering cross-sections of the pure atoms. In this manner, the number of required simulations is drastically reduced to only 2 for a binary column. The availability of this atomic lensing model in combination with some prior knowledge about the shape of the nanostructure enables one to retrieve the number of atoms in heterogeneous systems. This is illustrated here for an experimental ADF STEM image of a Au@Ag core-shell nanorod. For this structure, prior knowledge on the total thickness of the mixed atomic columns is required. In this manner, the number of variables that has to be predicted is limited. For this purpose, the total thickness in the mixed atomic columns was estimated by fitting a thickness profile based on the atom-counting results in the pure Ag shell regions. Next, by further exploiting the core-shell nature of the mixed columns, the number of Ag and Au atoms can be computed from the direct comparison between the measured experimental scattering cross-sections and predicted values. The atom-counting results for both types of atoms are shown in Fig. 3(b-c).

In order to avoid prior knowledge about the overall shape and thickness of the nanorod, yet another approach is needed. Moreover, when the difference between the atomic numbers of elements decreases, the detection of compositional differences in ADF STEM becomes increasingly more challenging or even impossible. For this purpose, HAADF STEM imaging can be combined with energy dispersive X-ray spectroscopy [34, 35]. Next to the HAADF STEM image, at each probe position the resultant X-ray emission spectrum is recorded. These spectra can then be used to construct elemental maps from which EDX scattering cross-sections can be estimated. Recently presented a new methodology to count the number of atoms in multimetallic nanocrystals by combining the HAADF STEM image and the elemental maps [34]. Due to the low SNR in the individual EDX elemental maps, the scattering cross-sections in the EDX images are measured using Voronoi cells. With this approach, each pixel is assigned to the nearest atomic column, with the positions of the atomic columns being determined from the simultaneously recorded HAADF STEM images. A simple linear scaling between the STEM and EDX scattering cross-sections can be assumed, which has been confirmed theoretically and experimentally [34, 36]. The monotonic increase of both EDX and HAADF STEM scattering cross-section values can be used to count the number of atoms. For this purpose, the measured scattering cross-sections are matched to simulated library values. The library values for the HAADF STEM scattering cross-sections of the mixed atomic columns are generated using frozen lattice image simulations of the pure element crystals [37, 38] in combination with the atomic lensing model [33]. As demonstrated by Zhang et al. [36], the atomic lensing model can also be used to predict EDX scattering cross-sections. The main challenge is to estimate the two scaling parameters for the EDX cross-sections of the two types of elements. It is assumed that the experimental HAADF scattering cross-section requires no scaling with respect to simulation [17, 25, 26]. For a single atomic column, because of the unknown EDX scal-

ing parameters, there is an ambiguity between sample thickness and composition. It is, however, possible to determine an upper and lower bound to the thickness from the HAADF scattering cross-section by assuming the column is either entirely the lighter or heavier species respectively. For each possible thickness, only one column composition can then match the HAADF scattering cross-section, allowing the EDX scaling parameters to be determined for that composition. By repeating this for all possible thicknesses compatible with the HAADF scattering cross-section, it becomes clear that a finite range of possible EDX scaling parameters for that single column is possible. For a sample with variations in thickness and composition, different columns will lead to different possible ranges of scaling parameters. With sufficient atomic columns in an experiment, the scaling parameters that are most compatible with all of the columns can be determined.

To explore the possibilities, simulated HAADF STEM images and EDX maps of a Au@Pt core-shell nanorod were analysed. For the EDX signals, the ionisation potential of the 2p orbitals of Pt and Au was used in the multislice simulations to create the elemental maps. The infinite dose simulations are shown in Fig. 4(a). The ground truth number of atoms (Fig. 4(b)), estimated number of atoms (Fig. 4(c)), and difference maps (ground truth - estimated) Fig. 4(d)) are also presented in Fig. 4. The observed differences in the atom-counting results are directly related to the unavoidable small mismatch between the simulated library of scattering cross-sections assuming the bulk unit cell and the measured scattering cross-sections from the relaxed Pt-Au nanorod. Next, the simulation set-up is made similar to an experimental set-up corresponding to EDX mapping of 60 min where the results are stored every 5 min followed by the acquisition of a HAADF STEM image. For this purpose a time series of 12 images is generated. After that, Poisson noise (50 noise realizations) is included in the simulated HAADF STEM image and the EDX elemental maps in order to evaluate the effect of a limited incident electron dose on the obtained counting results. For the HAADF STEM image an incident electron dose of 5×10^4 e^-Å^{-2} per frame is used and for the EDX elemental maps 5×10^6 e^-Å^{-2}. An example of such a simulated dataset is shown in Fig. 4(e) for a collection efficiency of 5%. The angular efficiency of our SuperX system is $0.7Sr/(4\pi)$, which is about 5%. The RMSE per atomic column for 5% efficiency is shown in Fig. 4(f). From this figure, it can be observed that the RMSE reaches values up to 3 for the number of Pt and Au atoms in the mixed atomic columns, but is less on average. The introduction of new instruments with an angular efficiency toward $4Sr/(4\pi) \approx 30\%$ [67,70] will greatly benefit quantification at the atomic level. This new type of detector will also bring new capabilities to study more beam-sensitive nanostructures, such as light element structures, for which limiting the incident electron dose during imaging is essential.

4. From 2D to 3D

In a next step, one of the objectives is to use the atom-counts to retrieve the atomic structure in three dimensions. Back in 2011, this has been done for the first time to determine the 3D atomic structure of a Ag particle embedded in an Al matrix as illustrated in Fig. 5 [16]. To achieve this result, two ADF STEM images were acquired under two different viewing directions. From these images, the number of Ag atoms in each column was counted. By combining the atom-counting results of the same particle from the two viewing directions, the 3D structure could be retrieved using discrete tomography.

When studying extremely beam sensitive nanostructures or changes over time, acquiring STEM images from different viewing directions to obtain the 3D structure is far from straightforward. Therefore, another alternative was developed, which circumvents these issues by reconstructing 3D atomic models from a single projection [21, 39, 41–43]. For this purpose, the atom-counting results are used to create an initial 3D atomic model. Next, an energy minimisation procedure can be applied to obtain a relaxed 3D reconstruction of the nanoparticle. In order to validate this method, this single projection reconstruction approach is compared with tomography [39]. For this purpose, three projection ADF STEM images of a Au nanorod were acquired along different major zone axes. These three projection images were used as an input for a 3D reconstruction using a compressive sensing based reconstruction technique [44]. For the atom-counting/energy-minimisation approach only one of those projection images is used to count the number of atoms. Based on the atom-counting results, an initial 3D configuration can be obtained by positioning the atoms in each atomic column, parallel to the beam direction, symmetrically around a central plane. The atoms are separated by a fixed distance a for the [100] orientation (or $a/\sqrt{2}$ for the [110] orientation) - where a = 4.078 Å is the lattice parameter of gold. In addition, prior knowledge about the [100] (or [110]) specimen orientation can be included. For example, for the [110] orientation the atomic position at even planes are shifted along the beam direction by $a/(2\sqrt{2})$ with respect to the odd planes. The relative heights of the atomic columns are then relaxed using a Monte Carlo approach using a Lennard-Jones potential [21]. Fig. 6 shows the comparison between the two atomic resolution reconstruction methods. Fig. 6(a,b) show the compressive sensing based reconstruction visualized along the [001] and [110] directions respectively, and similarly Fig. 6(c,d) show the reconstruction based on the atom-counting/energy-minimization approach. Both reconstructions are overlapped in Fig. 6(e,f) and an excellent visual match of the overall morphology of the nanorod has been found. The same excellent agreement between 3D reconstructions obtained using conventional high resolution electron tomography and the methodology based on atom counting and relaxation was also obtained for Pt nanoparticle of 10 nm [45]. The comparison between the atom-counting/energy-minimization approach and state-of-the-art electron tomography validates that a trustworthy 3D reconstruction can be obtained from a single image, where we can make reasonable assumptions that we are viewing a roughly symmetrical particle with no voids.

More recently, a lot of effort has been put in order to improve this atom-counting/energy minimisation method to overcome the limitations of the different possible approaches that are available for an energy minimisation. Mainly two strate-

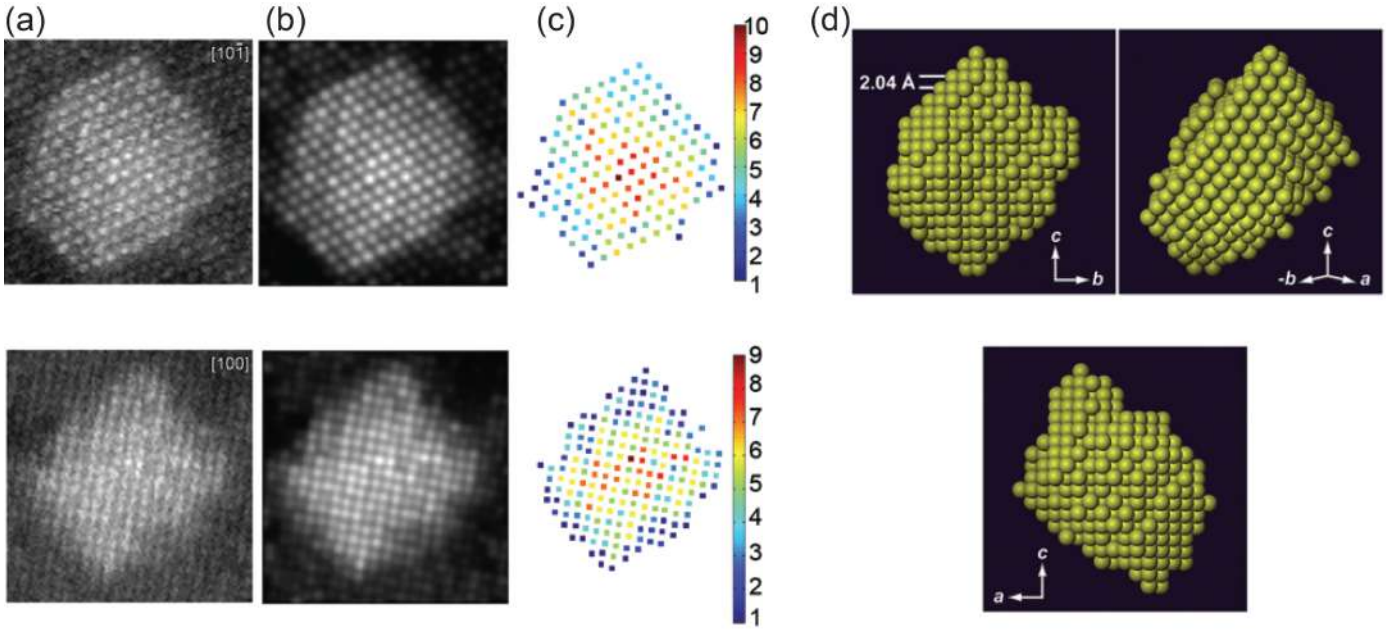

Figure 5: Atomic imaging of crystalline nanoparticles in three dimensions. (a) Experimental HAADF STEM images of nanosized Ag clusters embedded in an Al matrix in [10$\bar{1}$] zone-axis orientation and [100] zone-axis orientation. (b) Refined models of the images in (a). (c) Number of Ag atoms per column. (d) The computed 3D reconstruction of the Ag nanocluster viewed along three different directions. Reproduced from [16] with permission from Nature Publishing Group.

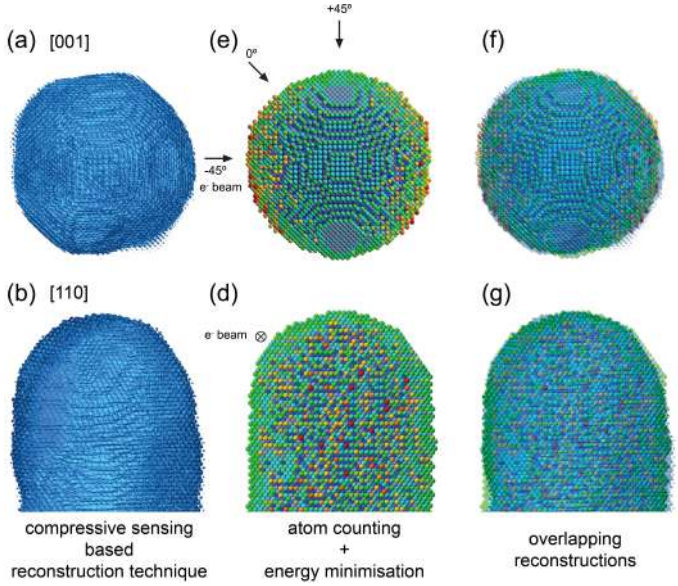

Figure 6: Comparison of the reconstructions based on atom counting with energy minimization and those obtained by atomic resolution tomography. (a, b) Compressive sensing based reconstruction of a Au nanorod viewed along [001] and [110] direction. (c, d) Reconstruction based on atom counting and energy minimization using a single projection image viewed along [001] and [110] orientation (the colouring of the Au atoms indicates the nearest-neighbour coordination, from 1 in red to 12 in dark blue). (e, f) Overlap of the reconstructions shown in (a, c) and (b, d). Adapted from [39] with permission from The Royal Society of Chemistry.

gies can be distinguished here. Using the first approach, which was also applied for the Au nanorod of Fig. 6, the energy is minimized by shifting the atomic columns up and down while keeping the number of atoms in a column fixed to the outcome of the atom-counting procedure [21, 39, 42, 43]. The second approach consists of a full molecular dynamics simulation to relax the particle's structure [39, 45, 47]. The first method is potentially too restrictive by ignoring the finite atom-counting precision, especially at lower doses. On the other hand, the second method runs the risk of ending up in a global energy minimum and violating the physical constraints of the experimental observation.

In order to avoid that purely computational energy minimisation approaches result in a close local minimum where the reconstructed structure may deviate from the experimental observation, the energy landscape can exhaustively be explored to find the local minimum corresponding to the experimentally observed structure. For this purpose, an iterative local minima search algorithm [48] was proposed which is followed by a molecular dynamics structural relaxation of candidate structures associated with each local minimum [40]. In this manner, it becomes possible to investigate the 3D atomic structure of supported nanoparticles, which may deviate from their ground state configuration. This new method was applied to experimental images of supported Au nanoparticles at high temperature and validated on a simulated system. The method is illustrated for the simulated system in Fig. 7. In the first step, Fig. 7(a), a starting model is build based on the atom-counting results obtained from the simulated ADF STEM image of the supported Au nanoparticle. Next the iterative local minima search algorithm to reconstruct the final 3D structure from the starting input model is applied. In this manner, a broad sampling of the energy landscape is provided, which is shown by the grey line in Fig. 7(b). From this landscape, local minima

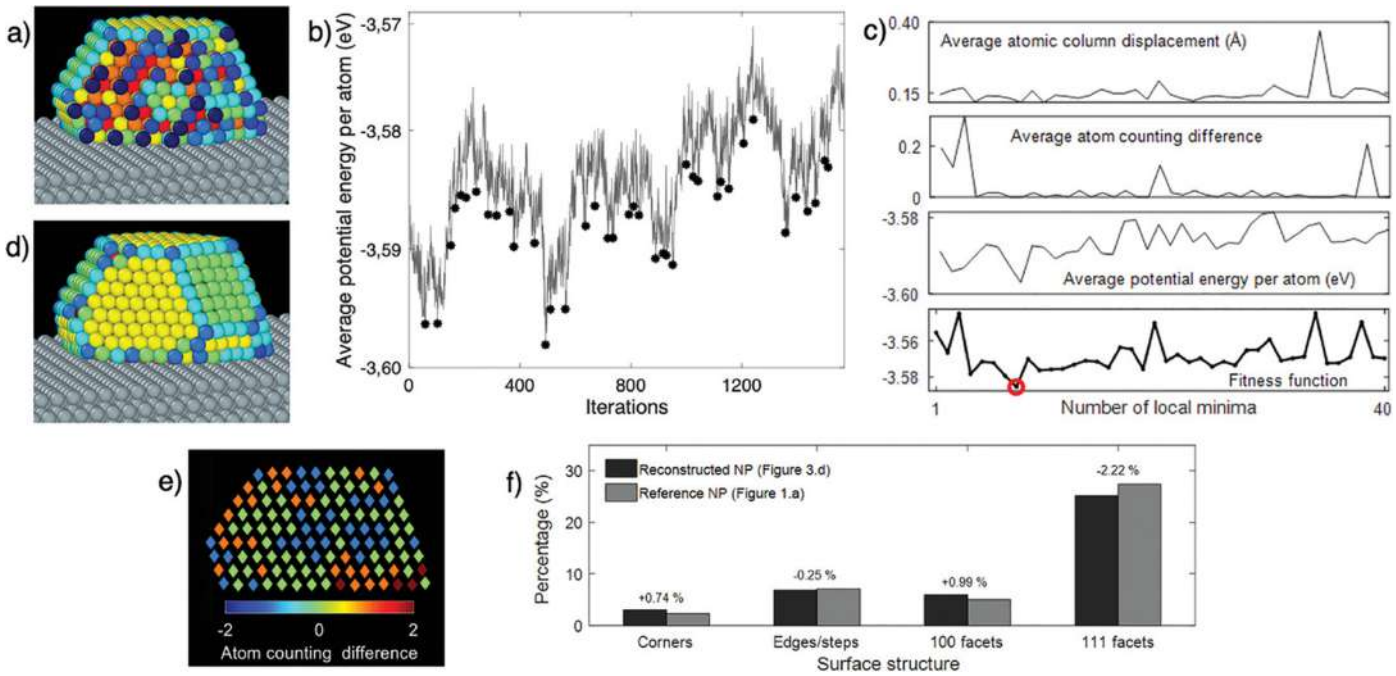

Figure 7: Main steps of the iterative local minima search algorithm demonstrated for a simulated Au nanoparticle. a) Starting 3D model created based on the atom-counting results. b) Neighbourhood energy landscape obtained by the iterative local minima search algorithm. c) The components of the defined fitness function. d) Reconstructed final Au nanoparticle on the support. Au atoms are presented in different colours according to their coordination numbers (see Figure 1a). e) Difference in number of atoms in each projected atomic column between the original input and reconstructed model. f) Comparison of the surface structure of the reconstructed nanoparticle and the original nanoparticle. The histogram is obtained from the coordination numbers of the atoms. Reprinted with permission from [40] Copyright (2021) John Wiley and Sons.

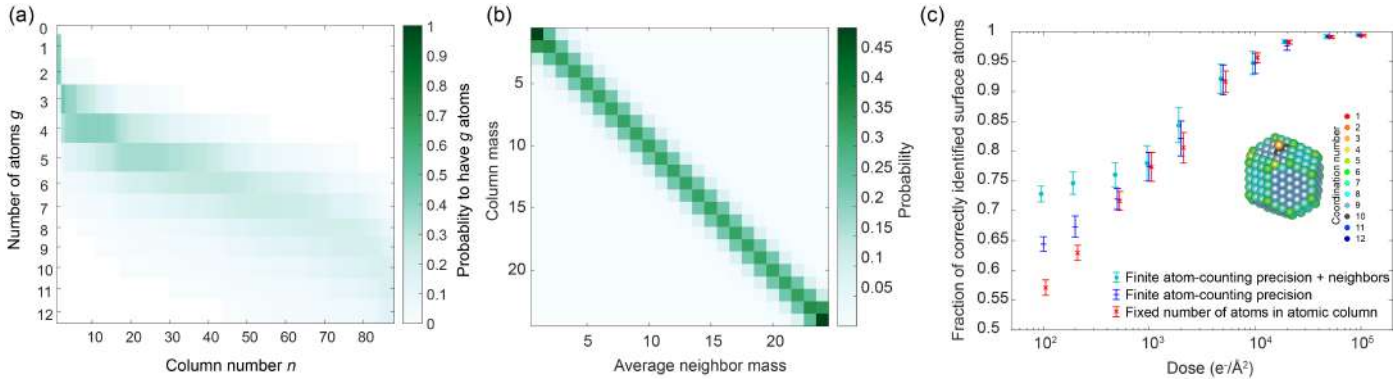

Figure 8: (a) Probability matrix showing the probability that the nth scattering cross-section has g atoms. (b) Neighbour-mass probability matrix showing the average mass of the neighbouring columns on the x-axis and the column mas on the y-axis. (c) Fraction of the correctly reconstructed surface atoms as a function of the incident electron dose. The inset shows the ground truth reconstruction of the Pt nanoparticle where the colouring of the Pt atoms indicates the nearest-neighbour coordination. Reproduced figure from [46] (Creative Commons CC BY license).

have been selected. They are indicated by the black dots in Fig. 7(b) and correspond to points that have the lowest value in regions where at least ten previous points showed a continuous decreasing trend. Next each candidate structure associated with a local minimum was relaxed by molecular dynamics simulations in a canonical ensemble at the experimental temperature. After this relaxation, the most plausible 3D structure is determined based on a fitness function which does take into account the difference with the experimental observations as well. Therefore, the fitness function consists of different contributions, i.e. (1) the average shift in the projected atomic column positions of each candidate model compared to the atomic column positions observed in the simulated ADF STEM image (2) the average difference between the number of atoms in each projected atomic column of the candidate solution and the estimated atom-counting results from the simulated ADF STEM image, and (3) the average potential energy per atom. The different contributions of the fitness function, and the overall fitness function are displayed for the different local minima in Fig. 7(c). The minimum value in the fitness graph (indicated with a red circle in Fig. 7(c)) provides the final 3D structure, which is shown in Fig. 7(d). The reconstructed model is quanti-

tatively evaluated by comparing it with the ground truth model. Fig. 7(e) shows the difference in the number of atoms in each projected atomic column between the reconstructed nanoparticle and original input model. The maximum difference equals ±2 atoms and is far less on average. Next to comparing the number of atoms in each atomic column, also the surface structure was quantitatively evaluated. The comparison of the surface structure of the reconstructed nanoparticle and the original 3D model is shown in Fig. 7(f). According to the results, it can be concluded that the surface structure of the reconstructed Au nanoparticle has been identified with an accuracy of more than 95% where the maximum difference of 2.22% was observed in the percentage of 111 facets as indicated in Fig. 7(f). This validates that supported Au nanoparticle at high temperatures can be accurately reconstructed with this method. Moreover, in this work [40], the new methodology is compared with previously reported approaches from which it could be concluded that the local search minima algorithm outperforms the previous approaches.

In parallel, another improved 3D atom-counting/energy minimisation reconstruction algorithm was developed [46]. This algorithm focuses on incorporating the finite atom-counting precision via a Bayesian inference scheme to improve the 3D atomic models for small nanostructures. Bayesian methods are powerful tools in which a priori information is rationally combined with the observed data and have been successful in other fields of science. Next to the finite atom-counting precision, the incorporation of additional prior knowledge from neighbour-mass relations is beneficial when reconstructing atomic models from extremely low dose ADF STEM images. This prior knowledge is fused into a genetic algorithm which uses atom-counting results as an input for reconstructing the 3D atomic structure. Genetic algorithms are typically used as efficient tools for solving large optimization problems where finding a direct solution is not possible [49, 50]. As an input for the reconstruction algorithm we need the probability that the nth atomic column contains a specific number of atoms $p(g|SCS_n)$. This can be defined as:

$$p(g|SCS_n) = \frac{p(g)p(SCS_n|g)}{\sum_g p(g)p(SCS_n|g)} \tag{4}$$

where $p(SCS_n|g)$ is the normal distribution describing the probability that component g generates the nth scattering cross-sections, given by the gth normal component of Eq.(2), and $p(g)$ the probability of having g atoms in a column, for which equal probabilities are assumed. The probability $p(g|SCS_n)$ can be visualised in a matrix. An example of such a probability matrix is shown in Fig. 8(a). This probability can also be used to represent the uncertainty of the atom-counting results [51]. For improving the quality of the reconstructions further at lower doses, a neighbour-mass matrix is constructed which helps to predict the column mass based on the average mass of the neighbouring columns. For small, convex nanoparticles, abrupt discontinuities are indeed highly non-physical. This matrix $p(g|NB_n)$ is chosen to be diagonal and is visualised in Fig. 8(b). Both probability matrices can be combined as

$$p\left(g|\mathrm{SCS}_n \cap \mathrm{NB}_n\right) = \frac{p(g|\mathrm{SCS}_n)p(g|\mathrm{NB}_n)}{\sum_g p(g|\mathrm{SCS}_n)p(g|\mathrm{NB}_n)} \tag{5}$$

where NB_n indeicates the average neighbour-mass of the nth column. This prior knowledge is inserted in the cost function of the genetic algorithm which evaluates the different candidate solutions. The cost-function χ is given by:

$$\chi = \frac{\sum E_a}{\sum_n g_n} \cdot \left(1 + \sqrt[n]{\prod_n p(g_n|\text{prior knowledge})}\right), \tag{6}$$

where $\sum E_a$ is the sum of the energies per atom given by the EAM potential [52, 53] and $\sum_n g_n$ is the total particle mass. This cost-function consists of two factors where the first represents the average energy per atom which we wish to minimize. The second factor allows to penalize the energy per atom with the probability of the candidate solution based on the prior knowledge (Eq.(4) or Eq.(5)), hence the name Bayesian genetic algorithm. In an extensive simulation study, the quality of the obtained reconstructions is quantitatively evaluated in terms of the surface atoms, which are of general interest for catalysis. Fig. 8(c) shows the fraction of correctly reconstructed surface atoms of a simulated Pt nanoparticle. As a reference, the results for the reconstructions without prior knowledge are also included. A significant, targeted improvement for the reconstructed surface atoms is observed for the lower incident electron doses when including the finite atom-counting precision and the neighbour-mass relations.

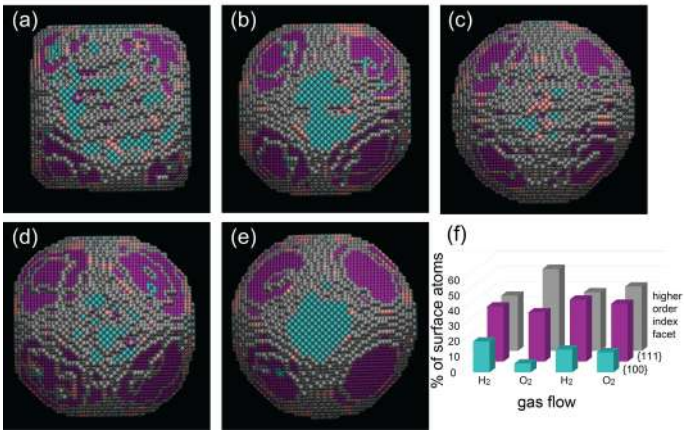

Figure 9: Structural evolution of Pt nanoparticles under different environmental conditions. Morphology of a Pt nanoparticle in vacuum (a) and in different gaseous environments, that is, (b,d) in 5% H2 in Ar; (c,e) in O2, all at 300 °C. The atoms are presented in different colours, according to the type of surface facet: blue = 100, pink = 110, purple = 111, gray = higher index. (f) Occurrence of different surface facets as a function of the gas flow in time. Note that a smaller, but constant presence of 110 facets was found for the different gaseous environments (not shown in this graph). Reproduced figure from [45].

5. Nanoparticle dynamics

The methodology of retrieving the 3D atomic reconstruction based on the atom-counting results opens new prospects

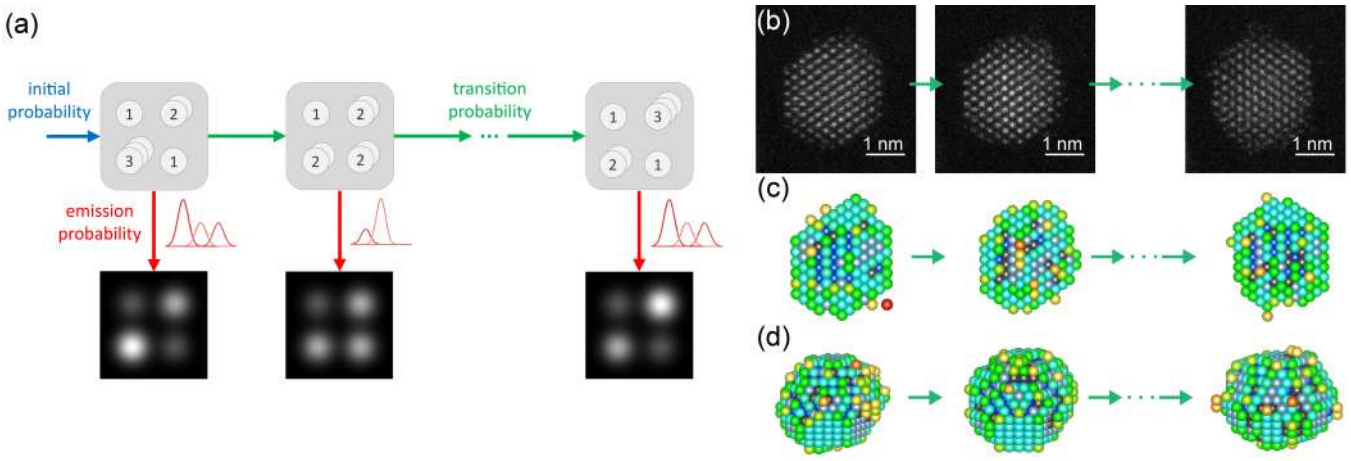

Figure 10: (a) The hidden Markov model for atom-counting models the number of atoms in each atomic column of the nanoparticle as the hidden states (top row) and the scattering cross-sections obtained from the ADF STEM images as the observations (bottom row). Reprinted figure with permission from [54] Copyright (2020) by the American Physical Society. (b) Analysis of an experimental ADf STEM time series of a catalyst Pt nanoparticle. (c) Corresponding reconstructed 3D atomic models for the time sequence viewed along the beam direction. (d) Rotated models to show the dominant surface facets. The colouring of the atoms corresponds to the nearest-neighbour coordination, from 1 in red to 12 in dark blue. Reproduced figure from [46] (Creative Commons CC BY license).

for the characterisation of beam-sensitive materials or where the acquisition of a tilt series is impossible, such as dynamical processes. One of the applications is the quantification of the refaceting of Pt nanoparticles with atomic resolution during various oxidation-reduction cycles [45]. Fig. 9(a) shows the reconstructed 3D structure of a Pt nanoparticle in vacuum. Fig. 9(b-e) shows the behaviour of a similar particle in different gas environments. The in situ experiment was performed at 300°C and the gas flow was varied from vacuum to 1 bar of 5% H_2 in Ar flow (Fig. 9(b)), and subsequently to a 1 bar O_2 environment (Fig. 9(c)), corresponding to conditions which are similar to those typically used during reduction and oxidation reactions. To investigate the behaviour of the nanoparticle during continuous reducing-oxidizing environments, we switched once more the gas flow to 5% H_2 in Ar (Fig. 9(d)) and subsequently to O_2 (Fig. 9(e)). In vacuum, the particle shape corresponds to a truncated cube, whereas in H_2, the shape resembles a truncated octahedron(Fig. 9(b,d)). The morphology is found to become more rounded in an O_2 environment (Fig. 9(c,e)). Such information is critical to reveal the behaviour of the catalyst particle in a real working environment. Moreover, the number of 7-, 8-, and 9-coordinated surface atoms were quantified based on the reconstructed 3D atomic models. On the basis of these values, we can extract the occurrence of different types of surface facets, which is illustrated by the colour codes in Figure 9(f). The more faceted appearance of the particle in H_2 is reflected by the obvious presence of 100 and 111 planes. In O_2, we observe a decrease of the percentage of these facets and a significant increase of higher order facets, corresponding to a more rounded morphology. This methodology clearly enables a direct quantification of the real 3D morphological changes at an atomic scale in gaseous environments. However, in this example we obtained the 3D atomic structure models by analysing the underlying images frame by frame. One of the challenges now is to investigate if we can enhance the reliability in the results obtained by modelling the dynamics between successive frames.

In order to model this, a so-called hidden Markov model was introduced, which is schematically illustrated in Fig. 10(a) [54–57]. The hidden Markov model depends on a set of parameters including initial probabilities which define the probabilities for a column to have a specific number of atoms in a column. In the simplified example of Fig. 10(a), the probability to have 1 atom is twice as large as the probability to have 2 or 3 atoms in a column. Whereas the probability to have more than 3 atoms is equal to zero. The number of atoms in a column are the so-called hidden states which we can not measure directly. We observe them indirectly through the scattering cross sections obtained from the ADF STEM images. The emission probability defines the probability of the scattering cross sections. Given a certain number of atoms in a column, this is described by a normal distribution function. From this, we see that for one time step, the hidden Markov model is in fact equal to the Gaussian mixture model introduced in the statistics-based atom counting procedure. Instead of analysing a time series of images frame by frame, we will also estimate transition probabilities which in a sense model the dynamics of the nanoparticle. It defines probabilities for a given column of atoms to, for example, lose or gain an atom. Assumptions of the hidden Markov model are that the transition probabilities do not change over time and that the next state only depends on the previous state but not on the states before that. Using a maximum likelihood estimation algorithm, the goal is then to estimate the initial probabilities, emission probabilities and transition probabilities. Once the parameters of the model are estimated, the so-called Viterbi algorithm is used to indicate the most likely state sequence [54, 57–59].

This hidden Markov model approach has been applied to 25 frames of an experimental time series of a catalyst Pt nanoparticle (Fig. 10(b)) [46]. The atom-counting results from each

single frame were used as an in put for the Bayesian genetic algorithm introduced in the previous section. In this manner, prior knowledge about the finite atom-counting precision and the neighbour-mass relations was incorporated for the reconstruction of the 3D atomic models. The reconstructed models are schematically represented in Fig. 10(c) and (d).

6. Conclusions and outlook

The methodologies and examples discussed in this overview article demonstrate that atom-counting and 3D atomic modelling has successfully been applied to a variety of nanoparticles over the past decade. For some of the presented methods here, a substantial incident electron dose is needed or prior knowledge is required about the specimen under study. In order to go beyond these limitations, multimode atomic resolution ADF STEM might be a solution during which STEM images are acquired from different detector regions [60–64]. For this purpose, a great flexibility is provided by pixelated detectors [63, 65–68]. From a recorded 4D dataset, where for each probe position the 2D convergent beam electron diffraction pattern is acquired, multiple conventional STEM images can be reconstructed for different detector regimes corresponding to different inner and outer angles. Although the impact of inelastic, plasmon excitations at low scattering angles is still under investigation [60, 69, 70], we investigated the benefit of using multiple detector regimes to unscramble mixed element nanostructures in a preliminary study [71]. For this purpose, the optimal experiment design has been determined using the principles of detection theory [72–75]. If the signals from multiple detector regions need to be analysed collectively, an extension of the current one-dimensional Gaussian mixture model to a multivariate Gaussian mixture model would be logical. This extension would not only be helpful when analysing scattering cross-section data from different detector regimes, but also for combining spectroscopic signals such as EDX and EELS scattering cross-sections [36], with the ADF STEM scattering cross-sections within one framework. Furthermore, machine learning methods based on artificial neural networks [76] are becoming increasingly important for the electron microscopy community [77–80]. Such novel approaches hold great potential for quantitative analyses resulting in a precise characterisation of complex nanostructures over time and under realistic conditions in heating, liquid or gas flow experiments. These results are essential to obtain a deeper understanding in the structure-property relationship of materials. In other words, these developments will assist the design of materials with interesting properties which are predictable and producible.

Acknowledgements

This work was supported by the European Research Council (Grant 770887 PICOMETRICS to S. Van Aert, Grant 815128 REALNANO to S. Bals, and Grant 823717 ESTEEM3). The authors acknowledge financial support from the Research Foundation Flanders (FWO, Belgium) through project fundings (G.0267.18N, G.0502.18N, G.0346.21N, and EOS 30489208) and a postdoctoral grant to A. De Backer. S. Van Aert acknowledges funding from the University of Antwerp Research fund (BOF). The authors also thank the colleagues who have contributed to this work over the years, including T. Altantzis, E. Arslan Irmak, K.J. Batenburg, E. Bladt, A. De wael, R. Erni, C. Faes, B. Goris, L. Jones, L.M. Liz-Marzán, I. Lobato, G.T. Martinez, P.D. Nellist, M.D. Rosell, A. Rosenauer, K.H.W. van den Bos, A. Varambhia, and Z. Zhang.

References

[1] A. V. Crewe, J. Wall, J. Langmore, Visibility of Single Atoms, Science 168 (1970) 1338–1340.

[2] J. C. H. Spence, The future of atomic resolution electron microscopy for materials science, Materials Science and Engineering R26 (1999) 1–49.

[3] S. Van Aert, J. Verbeeck, R. Erni, S. Bals, M. Luysberg, D. Van Dyck, G. Van Tendeloo, Quantitative atomic resolution mapping using high-angle annular dark field scanning transmission electron microscopy, Ultramicroscopy 109 (2009) 1236–1244.

[4] A. Rosenauer, T. Mehrtens, K. Müller, K. Gries, M. Schowalter, P. V. Satyam, S. Bley, C. Tessarek, D. Hommel, K. Sebald, M. Seyfried, J. Gutowski, A. Avramescu, K. Engl, S. Lutgen, Composition mapping in InGaN by scanning transmission electron microscopy, Ultramicroscopy 111 (2011) 1316–1327.

[5] G. T. Martinez, A. Rosenauer, A. De Backer, J. Verbeeck, S. Van Aert, Quantitative composition determination at the atomic level using model-based high-angle annular dark field scanning transmission electron microscopy, Ultramicroscopy 137 (2014) 12–19.

[6] A. B. Yankovich, B. Berkels, W. Dahmen, P. Binev, S. I. Sanchez, S. A. Bradley, A. Li, I. Szlufarska, Voy, Picometre-precision analysis of scanning transmission electron microscopy images of platinum nanocatalysts, Nature Communications 5 (2014) 4155.

[7] H. Agrawal, B. K. Patra, T. Altantzis, A. De Backer, E. C. Garnett, Quantifying Strain and Dislocation Density at Nanocube Interfaces after Assembly and Epitaxy, ACS Appl. Mater. Interfaces 12 (2020) 8788–8794.

[8] N. Kirkwood, A. De Backer, T. Altanzis, N. Winckelmans, A. Longo, F. V. Antolinez, F. T. Rabouw, L. De Trizio, J. J. Geuchies, J. T. Mulder, N. Renaud, S. Bals, L. Manna, A. J. Houtepen, Locating and controlling the Zn content in In(Zn)P quantum dots, Chemistry of Materials 32 (2020) 557–565. doi:10.1021/acs.chemmater.9b04407.

[9] X. Luo, A. Varambhia, W. Song, D. Ozkaya, S. Lozano-Perez, P. D. Nellist, High-precision atomic-scale strain mapping of nanoparticles from STEM images, Ultramicroscopy 239 (2022) 113561.

[10] A. J. den Dekker, S. Van Aert, A. van den Bos, D. Van Dyck, Maximum likelihood estimation of structure parameters from high resolution electron microscopy images. Part I: A theoretical framework, Ultramicroscopy 104 (2005) 83–106.

[11] S. Van Aert, A. J. den Dekker, A. van den Bos, D. Van Dyck, J. H. Chen, Maximum likelihood estimation of structure parameters from high resolution electron microscopy images: Part II: A practical example, Ultramicroscopy 104 (2005) 107–125.

[12] A. De Backer, K. H. W. van den Bos, W. Van den Broek, J. Sijbers, S. Van Aert, StatSTEM: An efficient approach for accurate and precise model-based quantification of atomic resolution electron microscopy images, Ultramicroscopy 171 (2016) 104–116.

[13] H. E, K. E. MacArthur, T. J. Pennycook, E. Okunishi, A. J. D'Alfonso, N. R. Lugg, L. J. Allen, P. D. Nellist, Probe integrated scattering cross sections in the analysis of atomic resolution HAADF STEM images, Ultramicroscopy 133 (2013) 109–119.

[14] G. T. Martinez, A. De Backer, A. Rosenauer, J. Verbeeck, S. Van Aert, The effect of probe inaccuracies on the quantitative model-based analysis of high angle annular dark field scanning transmission electron microscopy images, Micron 63 (2014) 57–63.

[15] K. E. MacArthur, A. J. D'Alfonso, D. Ozkaya, L. J. Allen, P. D. Nellist, Optimal ADF STEM imaging parameters for tilt-robust image quantification, Ultramicroscopy 156 (2015) 1–8.

[16] S. Van Aert, K. J. Batenburg, M. D. Rossell, R. Erni, G. Van Tendeloo, Three-dimensional atomic imaging of crystalline nanoparticles, Nature 470 (2011) 374–377.

[17] S. Van Aert, A. De Backer, G. T. Martinez, B. Goris, S. Bals, G. Van Tendeloo, Procedure to count atoms with trustworthy single-atom sensitivity, Physical Review B 87 (2013) 064107.

[18] A. De Backer, G. T. Martinez, A. Rosenauer, S. Van Aert, Atom counting in HAADF STEM using a statistical model-based approach: methodology, possibilities, and inherent limitations, Ultramicroscopy 134 (2013) 23–33.

[19] J. M. LeBeau, S. D. Findlay, L. J. Allen, S. Stemmer, Standardless Atom Counting in Scanning Transmission Electron Microscopy, Nano Letters 10 (2010) 4405–4408.

[20] J. Hwang, J. Y. Zhang, A. D'Alfonso, L. J. Allen, S. Stemmer, Three-Dimensional Imaging of Individual Dopant Atoms in $SrTiO_3$, Physical Review Letters 111 (2013) 266101.

[21] L. Jones, K. E. MacArthur, V. T. Fauske, A. T. J. van Helvoort, P. D. Nellist, Rapid Estimation of Catalyst Nanoparticle Morphology and Atomic-Coordination by High-Resolution Z-Contrast Electron Microscopy, Nano Letters 14 (2014) 6336–6341.

[22] H. Katz-Boon, M. Walsh, C. Dwyer, P. Mulvaney, A. M. Funston, J. Etheridge, Stability of Crystal Facets in Gold Nanorods, Nano Letters 15 (2015) 1635–1641.

[23] H. Kim, J. Y. Zhang, S. Raghavan, S. Stemmer, Direct Observation of Sr Vacancies in $SrTiO_3$ by Quantitative Scanning Transmission Electron Microscopy, Physical Review X 6 (2016) 041063.

[24] G. McLachlan, D. Peel, Finite Mixture Models, Wiley series in probability and statistics, John Wiley and Sons, inc., 2000.

[25] J. M. LeBeau, S. Stemmer, Experimental quantification of annular dark-field images in scanning transmission electron microscopy, Ultramicroscopy 108 (2008) 1653–1658.

[26] A. Rosenauer, K. Gries, K. Müller, A. Pretorius, M. Schowalter, A. Avramescu, K. Engl, S. Lutgen, Measurement of specimen thickness and composition in $Al_xGa_{1-x}N$/GaN using high-angle annular dark field images, Ultramicroscopy 109 (2009) 1171–1182.

[27] T. Grieb, K. Müller, R. Fritz, M. Schowalter, N. Neugebohrn, N. Knaub, K. Volz, A. Rosenauer, Determination of the chemical composition of GaNAs using STEM HAADF imaging and STEM strain state analysis, Ultramicroscopy 117 (2012) 15–23.

[28] A. Rosenauer, M. Schowalter, STEMSIM - a New Software Tool for Simulation of STEM HAADF Z-Contrast Imaging, in: A. Cullis, P. Midgley (Eds.), Microscopy of Semiconducting Materials 2007, volume 120 of *Springer Proceedings in Physics*, Springer Netherlands, 2008, pp. 170–172.

[29] S. Van Aert, A. De Backer, L. Jones, G. T. Martinez, A. Béché, P. D. Nellist, Control of Knock-On Damage for 3D Atomic Scale Quantification of Nanostructures: Making Every Electron Count in Scanning Transmission Electron Microscopy, Physical Review Letters 122 (2019) 066101.

[30] A. P. Dempster, N. M. Laird, D. B. Rubin, Maximum likelihood from incomplete data via the EM algorithm (with discussion), Journal of the Royal Statistical Society B 39 (1977) 1–38.

[31] L. Jones, H. Yang, T. J. Pennycook, S. J. Marshall, S. Van Aert, N. D. Browning, M. R. Castell, P. D. Nellist, Smart Align - a new tool for robust non-rigid registration of scanning microscope data, Advanced Structural and Chemical Imaging (2015).

[32] K. H. W. van den Bos, L. Janssens, A. De Backer, P. D. Nellist, S. Van Aert, The atomic lensing model: New opportunities for atom-by-atom metrology of heterogeneous nanomaterials, Ultramicroscopy 203 (2019) 155–162.

[33] K. H. W. van den Bos, A. De Backer, G. T. Martinez, N. Winckelmans, S. Bals, P. D. Nellist, S. Van Aert, Unscrambling mixed elements using high angle annular dark field scanning transmission electron microscopy, Physical Review Letters 116 (2016) 246101. Accepted.

[34] A. De Backer, Z. Zhang, K. H. W. van den Bos, E. Bladt, A. Sánchez-Iglesias, L. M. Liz-Marzán, P. D. Nellist, S. Bals, S. Van Aert, Element Specfic Atom Counting at the Atomic Scale by Combining High Angle Annular Dark Field Scanning Transmission Eelectron Microscopy and Energy Dispersive X-ay Spectroscopy, Small Methods (2022).

[35] K. E. MacArthur, T. J. A. Slater, S. J. Haigh, D. Ozkaya, P. D. Nellist, S. Lozano-Perez, Quantitative Energy-Dispersive X-Ray Analysis of Catalyst Nanoparticles Using a Partial Cross Section Approach, Microscopy and Microanalysis 22 (2016) 71–81.

[36] Z. Zhang, I. Lobato, A. De Backer, S. Van Aert, P. D. Nellist, Fast generation of calculated ADF-EDX scattering cross-sections under channelling conditions (2022). URL: `arXiv:2209.07950`.

[37] I. Lobato, D. Van Dyck, MULTEM: A new multislice program to perform accurate and fast electron diffraction and imaging simulation using Graphics Processing Units with CUDA, Ultramicroscopy 156 (2015) 9–17.

[38] I. Lobato, S. Van Aert, J. Verbeeck, Progress and new advances in simulating electron microscopy datasets using MULTEM, Ultramicroscopy 168 (2016) 17–27.

[39] A. De Backer, L. Jones, I. Lobato, T. Altantzis, B. Goris, P. D. Nellist, S. Bals, S. Van Aert, Three-dimensional atomic models from a single projection using Z-contrast imaging: verification by electron tomography and opportunities, Nanoscale 9 (2017) 8791–8798.

[40] E. Arslan Irmak, P. Liu, S. Bals, S. Van Aert, 3D atomic structure of supported metallic nanoparticles estimated from 2D ADF STEM images: a combination of atom-counting and a local minima search algorithm, Small Methods 5 (2021) 2101150.

[41] S. Bals, M. Casavola, M. A. van Huis, S. Van Aert, K. J. Batenburg, G. Van Tendeloo, D. Vanmaekelbergh, Three-Dimensional Atomic Imaging of Colloidal Core-Shell Nanocrystals, Nano Letters 11 (2011) 3420–3424.

[42] J. J. Geuchies, C. van Overbeek, W. H. Evers, B. Goris, A. De Backer, G. P. Gantapara, F. T. Rabouw, J. Hilhorst, J. L. Peters, O. Konovalov, A. V. Petukhov, M. Dijkstra, L. D. A. Siebbeles, S. Van Aert, S. Bals, D. Vanmaekelbergh, In situ study of the formation mechanism of two-dimensional supperlattices from PbSe nanocrystals, Nature Materials 15 (2016) 1248–1254.

[43] J. L. Peters, K. H. W. van den Bos, S. Van Aert, B. Goris, S. Bals, D. Vanmaekelbergh, Ligand-Induced Shape Transformation of PbSe Nanocrystals, Chemistry of Materials 29 (2017) 4122–4128.

[44] B. Goris, S. Bals, W. Van den Broek, E. Carbó-Argibay, S. Gómez-Graña, L. M. Liz-Marzán, G. Van Tendeloo, Atomic-scale determination of surface facets in gold nanorods, Nature Materials 11 (2012) 930–935.

[45] T. Altantzis, I. Lobato, A. De Backer, A. Béché, Y. Zhang, S. Basak, M. Porcu, Q. Xu, A. Saánchez-Iglesias, L. M. Liz-Marzán, G. Van Tendeloo, S. Van Aert, S. Bals, Three-Dimensional Quantification of the Facet Evolution of Pt Nanoparticles in a Variable Gaseous Environment, Nano Letters 19 (2019) 477–481.

[46] A. De Backer, S. Van Aert, C. Faes, E. Arslan Irmak, P. D. Nellist, L. Jones, Experimental reconstructions of 3D atomic structures from electron microscopy images using a Bayesian genetic algorithm, npj Computational Materials 8 (2022) 215.

[47] P. Liu, E. Arslan Irmak, A. De Backer, A. De wael, I. Lobato, A. Béché, S. Van Aert, S. Bals, Three-dimensional atomic structure of supported au nanoparticles at high temperature, Nanoscale 13 (2021) 1770–1776.

[48] G. Rossi, R. Ferrando, Searching for low-energy structures of nanoparticles: a comparison of different methods and algorithms, Journal of Physics: Condensed Matter 21 (2009) 084208.

[49] D. E. Goldberg, Genetic Algorithms in Search, Optimization & Machine Learning, Addison-Wesley Longman Publishing Co., Inc., 1989.

[50] M. Mitchell, An Introduction to Genetic Algorithms, A Bradford Book The MIT Press, 1996.

[51] A. De wael, A. De Backer, C.-P. Yu, D. G. Sentürk, I. Lobato, C. Faes, S. Van Aert, Three Approaches for Representing the Statistical Uncertainty on Atom-Counting Results in Quantitative ADF STEM, Microscopy and Microanalysis (2022) 1–9. doi:`10.1017/S1431927622012284`.

[52] S. M. Foiles, M. I. Baskes, M. S. Daw, Embedded-atom-method functions for the fcc metals Cu, Ag, Au, Ni, Pd, Pt, and their alloys, Physical Review B 33 (1986) 7983.

[53] B.-J. Lee, J.-H. Shim, M. I. Baskes, Semi-emperical atomic potentials for the fcc metals Cu, Ag, Au, Ni, Pd, Pt, Al, and Pb based on first and second nearest-neighbor modified embedded atom method, Physical Review B 68 (2003) 144112.

[54] A. De wael, A. De Backer, L. Jones, A. Varambhia, P. D. Nellist, S. Van Aert, Measuring Dynamic Structural Changes of Nanoparticles at the Atomic Scale Using Scanning Transmission Electron Microscopy, Physical Review Letters 124 (2020) 106105.

[55] L. R. Rabiner, A Tutorial on Hidden Markov Models and Selected Ap-

plications in Speech Recognition, Proceedings of the IEEE 77 (1989) 257–286.
[56] Z. Ghahramani, M. I. Jordan, Factorial Hidden Markov Models, Machine Learning 29 (1997) 245–273.
[57] A. De wael, A. De Backer, S. Van Aert, Hidden Markov model for atom-counting from sequential ADF STEM images: Methodology, possibilities and limitations, Ultramicroscopy 219 (2020) 113131. doi:10.1016/j.ultramic.2020.113131.
[58] A. J. Viterbi, Error bounds for convolutional codes and an asympotically optimum decoding algorithm, IEEE Trans. Inf. Theory 13 (1967) 260.
[59] G. D. Forney, The Viterbi algorithm, IEEE Trans. Inf. Theory 61 (1973) 268.
[60] K. Müller-Caspary, O. Oppermann, T. Grieb, F. F. Krause, A. Rosenauer, M. Schowalter, T. Mehrtnes, A. Beyer, K. Volz, P. Potapov, Materials characterisation by angle-resolved scanning transmission electron microscopy, Scientific Reports 6 (2016) 37146.
[61] J. Y. Zhang, J. Hwang, B. J. Isaac, S. Stemmer, Variable-angle high-angle annular dark-field imaging : application to three-dimensional dopant atom profiling, Scientific Reports 5 (2015) 12419.
[62] N. Winckelmans, T. Altantzis, M. Grzelczak, A. Sánchez-Iglesias, L. Liz-Marzán, S. Bals, Multimode electron tomography as a tool to characterize the internal structure and morphology of gold nanoparticles, The Journal of Physical Chemistry C 122 (2018) 13522–13528.
[63] Y. Wen, C. Ophus, C. S. Allen, S. Fang, J. Chen, E. Kaxiras, A. I. Kirkland, J. H. Warner, Simultaneous Identification of Low and High Atomic Number Atoms in Monolayer 2D Materials Using 4D Scanning Transmission Electron Microscopy, Nano Letters 19 (2019) 6482–6491.
[64] C. Ophus, Four-Dimensional Scanning Transmission Electron Microscopy (4d-stem): From Scanning Nanodiffraction to Ptychography and Beyond, Microscopy and Microanalysis 25 (2019) 563–582.
[65] A. R. Faruqi, G. McMullan, Direct imaging detectors for electron microscopy, Nuclear Instruments & Methods in Physics Research, Section A: Accelerators, Spectrometers, Detectors, and Associated Equipment 878 (2018) 180–190.
[66] N. Shibata, Y. Kohno, S. D. Findlay, H. Sawada, Y. Kondo, Y. Ikuhara, New area detector for atomic-resolution scanning transmission electron microscopy, Journal of Electron Microscopy 59 (2010) 473–479.
[67] Z. Chen, M. Weyland, P. Ercius, J. Ciston, C. Zheng, M. S. Fuhrer, A. J. D'Alfonso, L. J. Allen, S. D. Findlay, Practical aspects of diffractive imaging using an atomic-scale coherent electron probe, Ultramicroscopy 169 (2016) 107–121.
[68] H. Yang, R. N. Rutte, L. Jones, M. Simson, R. Sagawa, H. Ryll, M. Huth, S. J. Pennycook, M. L. H. Green, H. Soltau, Y. Kondo, B. G. Davis, P. D. Nellist, Simultaneous atomic-resolution electron ptychography and Z-contrast imaging of light and heavy elements in complex nanostructures, Nature Communications 7 (2016) 2532.
[69] A. Beyer, F. F. Krause, H. L. Robert, S. Firoozabadi, T. Grieb, P. Kükelhan, D. Heimes, M. Schowalter, K. Müller-Caspary, A. Rosenauer, K. Volz, Influence of plasmon exciteations on atomic-resolution quantitative 4D scanning transmission electron microscopy, Scientific Reports 10 (2020) 17890.
[70] H. L. Robert, B. Diederichs, Müller-Caspary, Contribution of multiple plasmon scattering in low-angle electron diffraction investigated by energy-filtered atomically resolved 4D-STEM, Applied Physics Letters 121 (2022) 213502.
[71] D. G. Sentürk, A. De Backer, T. Friedrich, S. Van Aert, Optimal experiment design for element specific atom counting using multiple annular dark field scanning transmission electron microscopy detectors, Ultramicroscopy 242 (2022) 113626.
[72] S. M. Kay, Fundamentals of Statistical Signal Processing: Volume II Detection Theory, Prentice-Hall, Inc., New Jersey, 2009.
[73] A. J. den Dekker, J. Gonnissen, A. De Backer, J. Sijbers, S. Van Aert, Estimation of unknown structure parameters from high-resolution (S)TEM images: What are the limits?, Ultramicroscopy 134 (2013) 34–43.
[74] J. Gonnissen, A. De Backer, A. J. den Dekker, G. T. Martinez, A. Rosenauer, J. Sijbers, S. Van Aert, Optimal experimental design for the detection of light atoms from high-resolution scanning transmission electron microscopy images, Applied Physics Letters 105 (2014) 063116.
[75] A. De Backer, A. De wael, J. Gonnissen, S. Van Aert, Optimal experimental design for nano-particle atom-counting from high-resolution STEM images, Ultramicroscopy 151 (2015) 46–55.
[76] A. Krizhevsky, I. Sutskever, G. E. Hinton, Image classification with deep convolutional neural networks, Advances in Neural Information Processing Systems 25 (2012) 1097.
[77] M. Ziatdinov, O. Dyck, A. Maksov, X. Li, X. Sang, K. Xiao, R. R. Unocic, R. Vasudevan, S. Jess, S. V. Kalinin, Deep Learning of Atomically Resolved Scanning Transmission Electron Microscopy Images: Chemical Identification and Tracking Local Transformations, ACS Nano 11 (2017) 12742–12752.
[78] J. Madsen, P. Liu, J. Kling, J. B. Wagner, T. W. Hansen, O. Winther, J. Schiøtz, A Deep Learning Approach to Identify Local Structures in Atomic-Resolution Transmission Electron Microscopy Images, Advanced Theory and Simulations 1 (2018) 1800037.
[79] T. Friedrich, C.-P. Yu, J. Verbeek, T. Pennycook, S. V. Aert, Phase retrieval from 4-dimensional electron diffraction datasets, in: 2021 IEEE International Conference on Image Processing (ICIP), 2021, pp. 3453–3457. doi:10.1109/ICIP42928.2021.9506709.
[80] S. V. Kalinin, C. Ophus, P. M. Voyles, R. Erni, D. Kepaptsoglou, V. Grillo, A. R. Lupini, M. P. Oxley, E. Schwenker, M. K. Y. Chan, J. Etherige, X. Li, G. G. D. Han, M. Ziatdinov, N. Shibata, S. J. Pennycook, Machine learning in scanning transmission electron microscopy, Nature Reviews Methods Primers 2 (2022) 11.